Quantification of local Ising magnetism in rare-earth pyrogermanates $Er_2Ge_2O_7$ and $Yb_2Ge_2O_7$

Daniel M. Pajerowski,[1] K. M. Taddei,[1] L. D. Sanjeewa,[2,3] A. T. Savici,[1] M. B. Stone,[1] and J. W. Kolis[3]
[1]*Neutron Scattering Division, Oak Ridge National Laboratory, Oak Ridge, Tennessee 37831, USA*
[2]*Materials Science and Technology Division, Oak Ridge National Laboratory, Oak Ridge, Tennessee 37931, USA*
[3]*Department of Chemistry, Clemson University, Clemson, South Carolina 29643, USA*

(Received 23 September 2019; revised manuscript received 3 December 2019; published 15 January 2020)

Recently, a local-Ising-type magnetic order was inferred from neutron diffraction of the antiferromagnetic $Er_2Ge_2O_7$ (pg-ErGO) with an applied magnetic field. Here, we use neutron spectroscopy to investigate the energetics of pg-ErGO and the isostructural $Yb_2Ge_2O_7$ (pg-YbGO) to evaluate the adequacy of the local-Ising description. To begin, we generate a model of the magnetic structure of pg-YbGO using neutron diffraction and find a net ferromagnetic moment. While pg-ErGO and pg-YbGO have highly symmetric crystal structures ($P4_12_12$ tetragonal space group 92) with only one trivalent rare-earth magnetic site, the point symmetry of the rare-earth site is low with only a single symmetry element (point group C_1). For both compounds, the energy scale of the first excited state is large compared to the magnetic ordering temperature, suggesting Ising character. The ground-state Kramer's doublet of both compounds is dominated by the maximal m_J component. However, the low point group symmetry of the rare-earth site leads to finite mixing of all other m_J's, which suggests potential deviations from Ising behavior. Moreover, quasielastic scattering is observed deep in the ordered state of pg-ErGO and pg-YbGO that may be due to non-Ising behavior. The dominant magnetic interaction in both compounds is found to be magnetostatic by considering the magnetic excitations in the ordered state. From consideration of these data, the pg-YbGO is more Ising-like than pg-ErGO. Also, quantum multicritical points are anticipated with applied magnetic field in both compounds.

DOI: 10.1103/PhysRevB.101.014420

I. INTRODUCTION

The Ising model has a rich history in the study of cooperative phenomena and was originally invoked to understand the confusing nature of ferromagnetism [1]. More recently, Ising models have been identified as model systems to test quantum computers [2]. While the Hamiltonian that governs a given two-level system is often trivial to write down, e.g.,

$$H_{\text{Ising}} = -J \sum_{i} \sum_{\delta} S_i^z S_{i+\delta}^z \qquad (1)$$

(where the summation index i is over all sites, δ is over nearest neighbors, J is the interaction energy, and there are two states per site) solutions to these many-body problems are difficult and continue to be a topic of research [3]. Considering the impetus of the model, it is fitting that magnetic materials are a plentiful resource for experimental realizations of Ising Hamiltonians. The criterion for a magnetic Ising system is twofold: (i) the ground state must be a doublet that is well separated from other single-ion excited states (e.g., the first excited state energy $E_{0\rightarrow1}$ should be much larger than the thermal energy associated with the onset of magnetic order k_BT_N) and (ii) the interacting matrix elements mixing the ground-state doublet on different sites should be zero [4]. This second condition is more subtle to characterize than the first. In addition, a high degree of symmetry is useful during modeling so tractable Hamiltonians may be considered.

Rare-earth containing insulators have been used to realize magnetic Ising models in a variety of different lattices, as the interaction energies of $4f$ electrons may be weak in comparison to the anisotropy energies [5]. Here, we briefly review crystal symmetry, magnetic ion local symmetry, and $E_{0\rightarrow1}/k_BT_N$ for some related rare-earth systems. Rare-earth ethylsulfates are hexagonal with C_{3h} point symmetry for the magnetic ions [6], and possess extremely large $E_{0\rightarrow1}/k_BT_N$ values of 200 [7,8], 1600 [9,10], and >8000 [11,12] for dysprosium, erbium, and ytterbium, respectively. Rare-earth hexahydrates are monoclinic with $C_1 \approx D_{4d}$ symmetry for the magnetic ions [13], and also have large $E_{0\rightarrow1}/k_BT_N$ values of 350 [14] and 300 [14,15] for dysprosium and erbium, respectively. As a frame of comparison to some popular Ising magnets, $Dy_3Al_5O_{12}$, $DyPO_4$, $LiHoF_4$, K_2CoF_4 have $E_{0\rightarrow1}/k_BT_N$ values of 27, 20, 7, and 4, respectively [4]. The coupling matrix element condition is less described in the literature as it requires details of the single-ion wave functions and interaction energies. Rare-earth magnets with pyrochlore structures are an example of local-Ising systems and the emergent rules resulting from their geometrically frustrating lattice geometry dominate the magnetic properties, although such frustration makes the $E_{0\rightarrow1}/k_BT_N$ parameter less applicable in determining Ising character [16]. The pyrogermanate tetragonal $P4_12_12$ (space group #92) crystal structure, Fig. 1(a), is stable for the series between Tb and Lu with only one distinct rare-earth site (Wyckoff position 8b) in the unit cell [17,18]. Locally, the rare-earth ions are surrounded by seven oxygen atoms and there is only the identity point symmetry, Fig. 1(b). The three-dimensional connectivity of the rare-earth ions is visualized in terms of five nearest neighbors that have just three unique bond distances, Fig. 1(c). For the eight rare-earth sites there are four local anisotropy axes that are not along any particular coordinate axis such that throughout the unit cell the

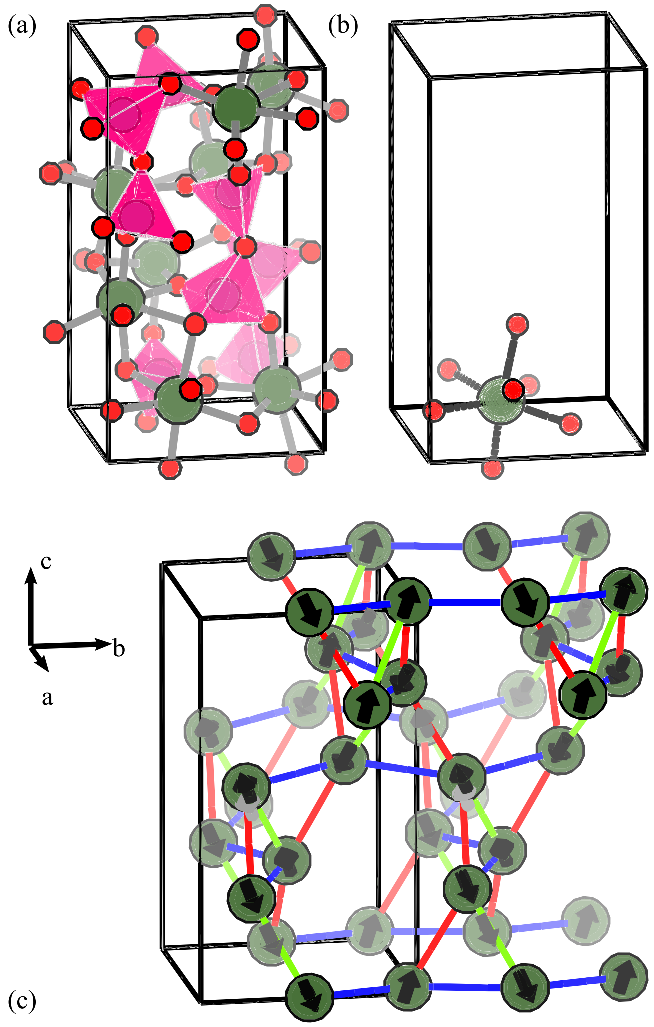

FIG. 1. Structure of pg-ErGO. (a) Crystal structure of one unit cell, where the erbium sites are represented by a large green circle, germanium is shown as the intermediately sized pink circle encapsulated by its coordinating tetrahedron, and oxygen is illustrated as the smallest red circle. (b) The local coordination sphere of erbium. (c) The magnetic structure is visualized with black arrows, and the nearest-neighbor erbium bond distances are shown as green (3.5743 Å), red (3.5961 Å), and blue (3.8014 Å). These images build on renderings by VESTA [25].

local-anisotropy axes are not always parallel. In this work we will provide $E_{0\rightarrow1}/k_BT_N$ values and investigate the non-Ising interaction mixing for pg-YbGO and pg-ErGO.

This paper focuses on inelastic neutron scattering of the putative local-Ising pyrogermanate $Er_2Ge_2O_7$ (pg-ErGO) and the isostructural $Yb_2Ge_2O_7$ (pg-YbGO). These pyrogermanate compounds have the same chemical formula as a pyrochlore structured material, but both the crystalline symmetry and the local symmetry of the rare-earth site are different. Recently, the magnetic structure of pg-ErGO was modeled as a function of applied magnetic field to reveal a local-Ising character with metamagnetism [19]. In this paper, we seek to better understand the nature of this local-Ising magnetism in pg-ErGO and compare with pg-YbGO.

Prior reports on magnetism within the rare-earth pyrogermanate family suggest the potential for Ising physics. Early work by Wanklyn provided a description of synthesis and structural characterization and indicated magnetic ordering temperatures of 2.05 K, 2.15 K, 1.45 K, and 1.15 K for the pyrogermanates $Tb_2Ge_2O_7$, $Dy_2Ge_2O_7$, $Ho_2Ge_2O_7$, and $Er_2Ge_2O_7$, respectively [18]. Soon after, optical absorption spectra were modeled using a crystal field Hamiltonian [20], and one description of the crystal field methodology is described in Ref. [21]. These optical data models can be extrapolated to give the energy levels of the ground-state terms, such that the first excited states are estimated as 8 meV ($E_{0\rightarrow1} \approx 90\,\mathrm{K}$) and 40 meV ($E_{0\rightarrow1} \approx 500\,\mathrm{K}$) for $Er_2Ge_2O_7$ and $Dy_2Ge_2O_7$, respectively, thus satisfying the first Ising model condition for magnetic materials. More recently, a model of a crystal field Hamiltonian based upon the magnetic susceptibility measurements of $Er_2Ge_2O_7$ predicted the first excited state to be 5 meV ($E_{0\rightarrow1} \approx 60\,\mathrm{K}$) above the ground-state doublet [22]. Notably, the aforementioned crystal field models used a limited parameter set of four terms, by approximating the local environment to have a fivefold rotation symmetry ($\approx D_{5h}$) about the vertical axis, which is nearly along the crystallographic c axis. In 2019, neutron diffraction measurements of pg-ErGO demonstrated an antiferromagnetic ground state, Fig. 1(c), with a first-order metamagnetic transition at $\approx 0.35\,\mathrm{T}$ for a field along the crystallographic a axis [19]. A study of the magnetothermodynamics of pyrogermanate $Dy_2Ge_2O_7$ [23] bears out an Ising-like description of the magnetization, although details of spin freezing and metamagnetism leave open questions. Similarly, the pyrogermanate $ho_2Ge_2O_7$ magnetic structure was reported and it along with the magnetization measurements indicate Ising-like behavior [24]. The magnetic structure of $Ho_2Ge_2O_7$ is different than that of pg-ErGO with each local magnetic moment rotated by 108° when going from one structure to the other, but there is consistency when considering the sign change of the α Steven's factor for Er^{3+} versus Ho^{3+} that gives rise to a 90° rotation of the anisotropy axis for uniaxial anisotropy dominated Hamiltonians [21]. This line of reasoning suggests two approximate sets of localizing axes for the rare-earth pyrogermanates with $\alpha < 0$ Ce, Pr, Nd, Tb, Dy, and Ho of one type and $\alpha > 0$ Pm, Sm, Er, Tm, and Yb of a second type. So, the rare-earth pyrogermanates bode well as a less studied lattice supporting Ising models against which to test the current theories.

In the following section, we use neutron scattering to quantify the Ising character of pg-ErGO and pg-YbGO. We first consider the magnetic structure of pg-ErGO and pg-YbGO with neutron diffraction, which yields the local anisotropy direction. Next, the paramagnetic, single-ion wave functions of pg-ErGO and pg-YbGO are modeled using excitations within the ground-state term probed by inelastic neutron scattering at temperatures that mainly populate the ground state but are above the magnetic ordering temperatures. These single-ion energy levels from neutron spectroscopy directly test the first criterion of Ising behavior, e.g., $E_{0\rightarrow1}/k_BT_N$ is large. The model-derived single-ion wave functions help test the second criterion of Ising behavior, to determine what matrix elements may connect interacting ions within the compounds. From this point, excitations within the ordered phase are considered, which provide observables that set the energy of magnetic interactions. A model based purely on magnetostatic interactions is posed. Finally, the results are summarized to quantify the degree of Ising character in these systems. Technical details are reported in Appendix A.

II. RESULTS AND DISCUSSION

A. Magnetic structures

To begin setting the stage to look for Ising magnetism, the ordered magnetic structure of pg-ErGO and pg-YbGO are considered. The magnetic structure of pg-ErGO was already reported [19], and here we present a model for the magnetic structure of pg-YbGO [26]. Both compounds were measured for inelastic studies using the cold neutron chopper spectrometer (CNCS) of the Spallation Neutron Source (SNS), and the elastic channel was isolated to model static magnetic contributions. The elastic magnetic contribution was further separated by subtracting $T = 1.5$ K data above magnetic ordering from $T = 0.1$ K data below magnetic ordering. The overall scale factor was taken from nuclear scattering of pg-YbGO data at 1.5 K, almost entirely from the (101) peak. The same scale factor was used for pg-ErGO after correcting for absorption, as there are no strong pg-ErGO nuclear peaks observable for the $E_\mathrm{i} = 1.55$ meV ($\lambda = 7.26$ Å) neutron energies used. Lattice parameters were fixed to the reported values for pg-ErGO [19]. For pg-YbGO, neutron powder diffraction data (Fig. 9) collected on the HB-2A neutron diffractometer of the High Flux Isotope Reactor were modeled to extract a structural model (Table VII) that is described in Appendix B, from which lattice parameters were fixed for magnetic structure refinements.

For both pg-YbGO and pg-ErGO, magnetic diffraction is observed with statistically significant intensities at positions commensurate with the parent crystallographic cell. Six different magnetic models were tested, and the ferromagnetic (along the c axis) irreducible representation Γ_3 was found to fit the data with the lowest residual for pg-YbGO while the antiferromagnetic Γ_2 was again found to best fit the pg-ErGO data, Table I. These data, modeled intensities, modeled residuals, and modeled magnetic structures are visualized in Fig. 2. For the best-fit models, the quantization axes of the

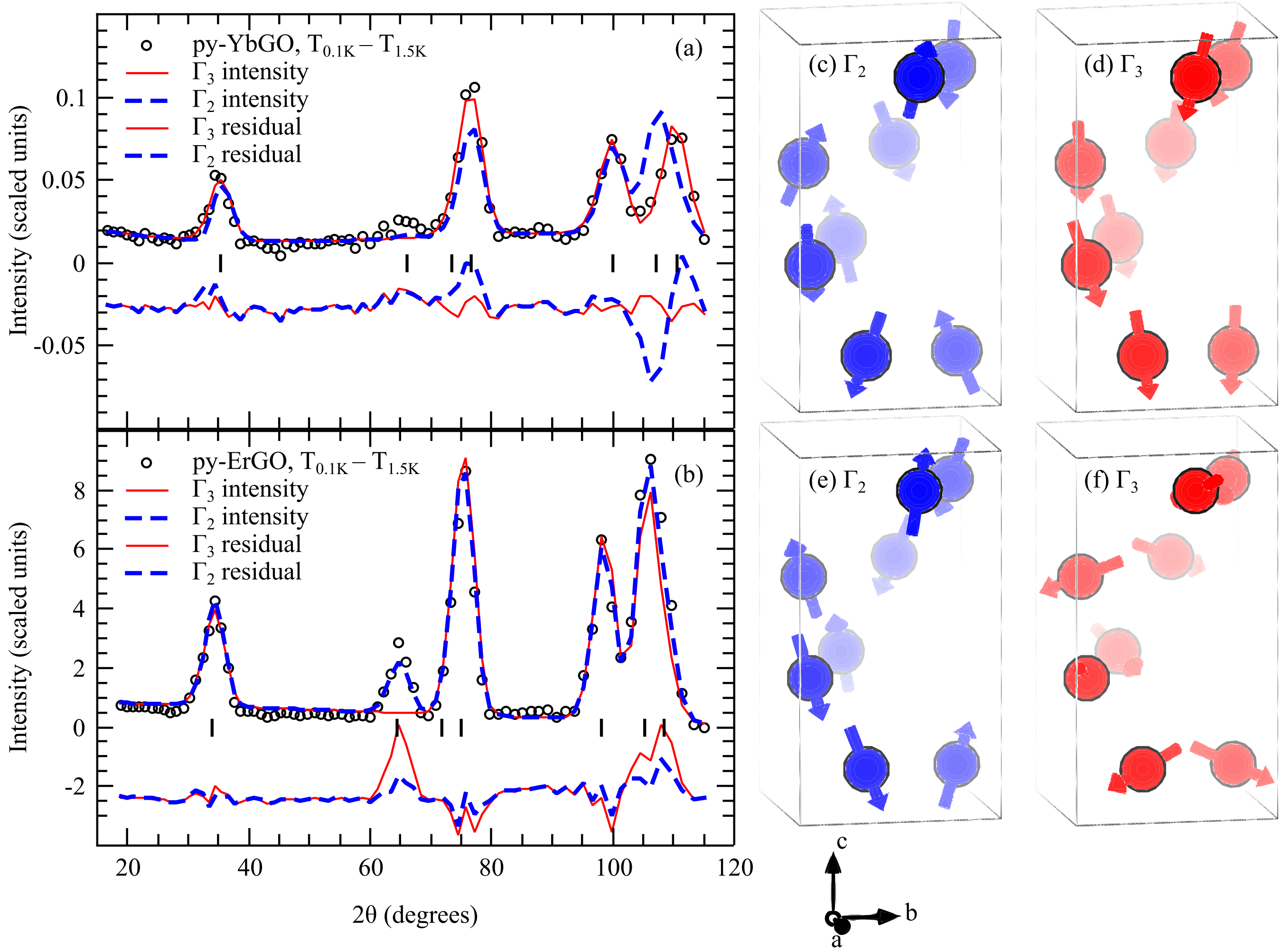

FIG. 2. Magnetic structures of pg-ErGO and pg-YbGO. The data are shown in comparison with the best-fit models of the two smallest R_{wp} Γ_2 and Γ_3 and the residuals for (a) pg-YbGO and (b) pg-ErGO. Tick marks identify reciprocal lattice vectors of (001), (100), (002), (101), (110), (102), and (111). The overall scale is the same, with different arbitrary offsets added to remove paramagnetic oversubtraction. Residuals are shown below data and models. The magnetic structures associated with the modeled intensities are shown for (c) pg-YbGO Γ_2, (d) pg-YbGO Γ_3, (e) pg-ErGO Γ_2, and (f) pg-ErGO Γ_3. The magnetic structure images build on renderings by VESTA [25].

TABLE I. Goodness of fit for magnetic structures. The weighted profile crystallographic R factor, R_{wp}, is listed for both compounds for each model. The best fit R_{wp} is highlighted for each compound.

Irreducible representation	Magnetic space group	pg-YbGO, R_{wp}	pg-ErGO, R_{wp}
Γ_1	$P4_12_12$	75.1	38.5
Γ_2	$P4'_12_12'$	43.4	**12.9**
Γ_3	$P4_12_12'$	**17.9**	26.2
Γ_4	$P4_12'_12$	46.4	43.6
Γ_5	$P2'_12'_12$	58.5	30.2
	$C22'2'_1$	47.3	30.6
	$P2'_1$		

moments are similar for both compounds and primarily along the c axis, Table II. The overall magnitude of the ordered erbium moment is found to be larger in the CNCS data than in the HB-2A data, and this difference may be due to errors in the scaling that assumes identical illumination and packing of pg-ErGO and pg-YbGO, the lower temperature of the CNCS measurement (0.1 K on CNCS versus 0.5 K on HB-2A) or a systemic issue with refining CNCS diffraction data. The ytterbium moment may be smaller than the maximally ordered moment, as there are no existing reports on the magnetic ordering temperature for pg-YbGO.

B. Single-ion Hamiltonians and wave functions

Neutron spectroscopy can directly measure the ground-state term energy levels of pg-ErGO and pg-YbGO and then be modeled to get single-ion wave functions, the results of which address the potential for Ising magnetism. So, a magnetic model for pg-ErGO is first built from the single-ion physics of the Kramers ion Er^{3+}. Trivalent erbium has eleven $4f$ electrons with the $^4\mathrm{I}_{15/2}$ ground-state ≈ 1000 meV lower in energy than the next state, $^4\mathrm{I}_{13/2}$ [5]. This spin-orbit-based splitting is not the aforementioned $E_{0\rightarrow1}$ energy, but rather shows the validity of only using the $^4\mathrm{I}_{15/2}$ term when analyzing the magnetic ground state. The interactions of the Er^{3+} $|J = 15/2\rangle$ state with the crystalline lattice due to electrostatic and bonding effects are parameterized in the crystal field formalism of Stevens that uses spherical harmonics up to $\ell = 6$ [21]. These crystal field split states of the $^4\mathrm{I}_{15/2}$ term are directly germane to the magnetic ground state, and it is the energy difference between the crystal field ground-state doublet and crystal field first-excited state doublet that is considered as the energy $E_{0\rightarrow1}$.

There is one Er^{3+} site in pg-ErGO (replicated eight times in the crystallographic unit as it is on the Wyckoff 8b position), and it has a C_1 symmetry. Previously, a single-ion Hamiltonian for pg-ErGO was fit to optical spectroscopy [20] and anisotropic magnetic susceptibility [22] measurements. This Hamiltonian assumed a dominant D_{5h} local symmetry, and while the available data were reproduced in each case, this simple model cannot account for the neutron scattering measurements. These pentagonally symmetric crystal field parameterizations were previously shown inconsistent with Mössbauer spectroscopy of pg-ErGO [27]. This D_{5h} symmetry is approximately along the c axis, with the five coordinated oxygen ions approximately in the ab plane.

Here, neutron spectroscopy was performed (on SEQUOIA of SNS) to further quantify the single-ion pg-ErGO wave function. By varying the Ei, the incident energy, (600 meV, 300 meV, 160 meV, 50 meV, 20 meV) at $T = 5\,\mathrm{K}$, a region of interest for the peaks between ≈10 meV and ≈60 meV was determined. A map of intensity as a function of sample energy transfer and momentum transfer magnitude for $E_\mathrm{i} = 160\,\mathrm{meV}$, $T = 5\,\mathrm{K}$ is shown in Fig. 3(a). Seven distinct, inelastic magnetic peaks are observed, and a model free fit of the $E_\mathrm{i} = 160\,\mathrm{meV}$, $T = 5\,\mathrm{K}$ intensities to resolution limited Gaussians shown in Fig. 3(b) gives the measured intensities reported in Table III. The magnetic character of these dispersionless excitations is confirmed by an agreement of the measured momentum dependence to that reported for the Er^{3+} magnetic form factor [28] in the dipolar approximation.

The $E_\mathrm{i} = 160\,\mathrm{meV}$, $T = 5\,\mathrm{K}$ peaks of pg-ErGO were modeled with no symmetry constraints to the crystal field Hamiltonian. The D_{5h} Hamiltonians are unable to reproduce the observed $T = 5\,\mathrm{K}$ neutron spectra, and the alleged pseudo-D_{5h} quantization axis does not align with the moment directions observed via neutron diffraction [19]. With no symmetry, there are 27 parameters (5 from $\ell = 2$, 9 from $\ell = 4$, and 13 from $\ell = 6$ terms), and there are ostensibly seven observables related to the peak positions and seven observables related to the peak intensities. A random initialization of $\mathrm{B}_{\ell m}$'s was found ineffective and instead a series of starting conditions for minimization were generated using point charge Hamiltonians with cutoff distances ranging from 3–20 Å. Each of these initial guesses were first subjected to a three-parameter fit scaling all $\ell = 2$, $\ell = 4$, and $\ell = 6$ terms together, and subsequently all parameters were minimized as described in Appendix A. The best-fit calculated solution is reported in Table III, with the parameters tabulated in Table VIII of Appendix C after rotating to maximize the expectation value of the J^z operator. A scale factor was applied to the measured intensity values when fitting to the model that results in absolute units. This fit reproduces all positions and intensities, except for an underestimated intensity of the 53 meV transition. It is not clear if this failure is of the model assumptions (e.g., a need for an even more highly parameterized Hamiltonian) or of the fitting procedure. The temperature dependence is

TABLE II. Ordered moments of best-fit models at $T = 0.1\,\mathrm{K}$. The $\hat{\mathrm{m}}$ unit vectors correspond to the local quantization axes of the ions.

beamline	compound	Γ	$\mathrm{m_a}$ (μ_B)	$\mathrm{m_b}$ (μ_B)	$\mathrm{m_c}$ (μ_B)	$\lvert\mathrm{m}\rvert$ (μ_B)	$\hat{\mathrm{m}}$
Hb2a [19]	pg-ErGO	Γ_2	2.66	3.03	–6.98	8.06	[0.33, 0.38, -0.87]
CNCS	pg-ErGO	Γ_2	2.15	3.11	–8.52	9.32	[0.23, 0.33, -0.91]
CNCS	pg-YbGO	Γ_3	0.31	0.09	–1.17	1.21	[0.26, 0.08, -0.96]

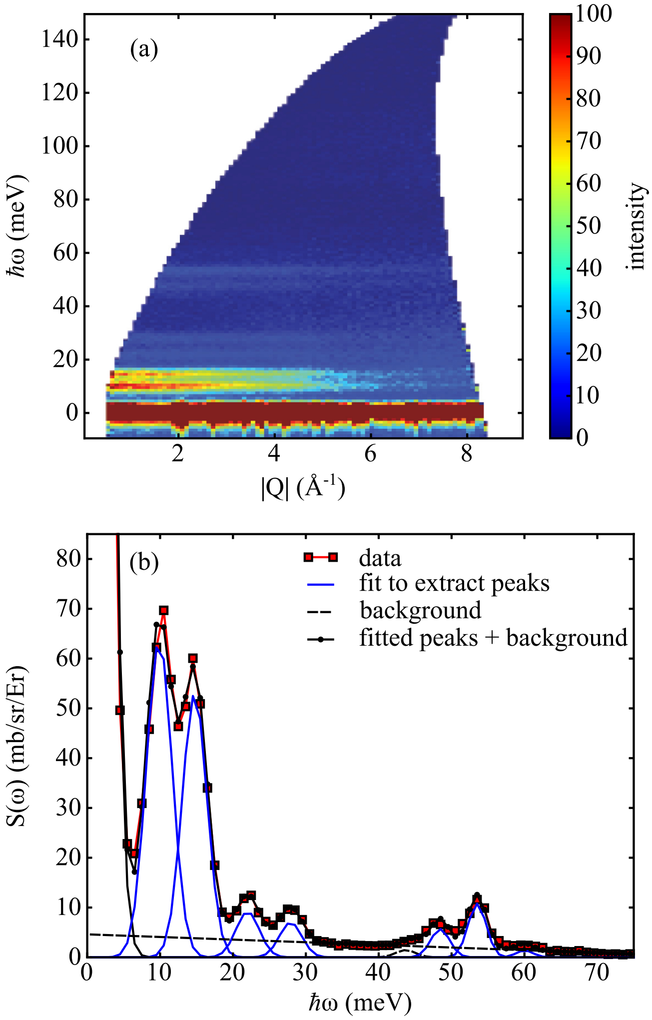

FIG. 3. High-energy neutron spectroscopy of pg-ErGO single-ion effects. Data are from SEQUOIA with $E_\mathrm{i} = 160\,\mathrm{meV}$ and $T = 5\,\mathrm{K}$. (a) An intensity map is shown with the isobar values in units of mb/sr/meV/Er. (b) An averaging of momentum transfers between $Q = [2, 4]\,\mathrm{Å}^{-1}$ with fits to resolution limited Gaussians.

semiquantitatively reproduced when heating to $T = 160\,\mathrm{K}$ and $T = 320\,\mathrm{K}$.

The ground-state pg-ErGO wave function associated with the best fit, using the maximum anisotropy axis as the quantization axis, is a Kramer's doublet dominated by $m_\mathrm{J} = \pm 15/2$ with nonzero contributions of all other m_j values, as reported in Table IX of Appendix C. This solution yields a ground-state moment of $8.514\,\mu_\mathrm{B} \pm 0.005\,\mu_\mathrm{B}$ (uncertainty is 1 standard deviation confidence interval from model fitting), which compares well to the measured ordered moment of $8.1\,\mu_\mathrm{B}$ at $T = 0.5\,\mathrm{K}$ [19]. These ground-state magnetic moments may be considered as local Ising from an energy scale consideration, as the first excited state is 114 K above the ground state with a $T_\mathrm{N} = 1.15\,\mathrm{K}$. For pg-ErGO the model is fairly well determined, as can be seen by the relative uncertainties.

A similar experimental procedure and analysis is possible for the pg-YbGO compound. Trivalent ytterbium has thirteen $4f$ electrons with the ${}^2\mathrm{F}_{7/2}$ state $\approx 1300\,\mathrm{meV}$ lower than the next spin-orbit state ${}^2\mathrm{F}_{5/2}$ [5], which motivates using the $J = 7/2$ manifold when considering the magnetic response. Within the crystal-field-split ${}^2\mathrm{F}_{7/2}$ states there is a spectrum for which the $E_{0\rightarrow 1}$ energy is defined. This $J = 7/2$ state then allows only four Kramers doublets, and the potential for three paramagnetic transitions from the ground state. From a modeling perspective, this decreased number of observables causes the pg-YbGO spectrum to be underdetermined.

One interpretation of single-ion physics in pg-YbGO is possible starting from the pg-ErGO parameters in Table VIII without any experimental constraints. These Er^{3+} parameters may be scaled to Yb^{3+} in the limit of zero covalency by taking the shielding parameters and radial matrix element expectation values from an electrostatic model [29] and including the Stevens factors [21]. The resulting Hamiltonian would have neutron transitions at energies of 28.8 meV, 82.7 meV, and 114.7 meV. The ground-state wave function associated with the scaled Hamiltonian has a magnetic moment of $3.04\,\mu_\mathrm{B}$. The disagreement between this scaling and the observed spectra suggests that covalency is important in these compounds. Previous crystal field analysis of bulk data that used the local D_{5h} symmetry also found poor scaling across different pyrogermanates [30].

This scaled pg-YbGO model may be tested with inelastic neutron scattering. By varying the incident energy (600 meV, 300 meV, 160 meV, 50 meV, 20 meV) at $T = 5\,\mathrm{K}$, a region of interest for the peaks between $\approx 20\,\mathrm{meV}$ and $\approx 80\,\mathrm{meV}$ was determined. A map of intensity as a function of sample energy transfer and momentum transfer magnitude for $E_\mathrm{i} = 160\,\mathrm{meV}$, $T = 5\,\mathrm{K}$ is shown in Fig. 4(a). Of the observed intensity peaks, only three were found to decrease intensity

TABLE III. Crystal field levels in pg-ErGO at $T = 5\,\mathrm{K}$, $E_\mathrm{i} = 160\,\mathrm{meV}$. Data are averaged over $Q = [2, 4]\,\mathrm{Å}^{-1}$. Measured and calculated $S_\mathrm{CF}(\omega)$ have the momentum dependent magnetic form factor contribution divided out. The uncertainties on measured quantities are 1 standard deviation confidence intervals from profiling the data in Fig. 3. The uncertainties on calculated quantities are 1 standard deviation confidence intervals of the model fitting.

transition	measured $\hbar\omega$ (meV)	calculated $\hbar\omega$ (meV)	measured $S_\mathrm{CF}(\omega)$ (mb/sr/Er)	calculated $S_\mathrm{CF}(\omega)$ (mb/sr/Er)
$0 \rightarrow 1$	9.85 ± 0.01	9.86 ± 0.01	424 ± 2	424 ± 2
$0 \rightarrow 2$	14.75 ± 0.01	14.765 ± 0.002	340 ± 2	340 ± 2
$0 \rightarrow 3$	21.97 ± 0.04	21.905 ± 0.005	59.1 ± 1.0	62.9 ± 0.3
$0 \rightarrow 4$	27.89 ± 0.04	27.860 ± 0.003	42.5 ± 0.9	41.5 ± 0.2
$0 \rightarrow 5$	48.13 ± 0.05	48.28 ± 0.01	24.6 ± 0.7	32.8 ± 0.2
$0 \rightarrow 6$	53.44 ± 0.04	53.54 ± 0.01	44.6 ± 1.4	25.1 ± 0.1
$0 \rightarrow 7$	60.45 ± 0.09	63.81 ± 0.01	4.2 ± 0.4	2.8 ± 0.1

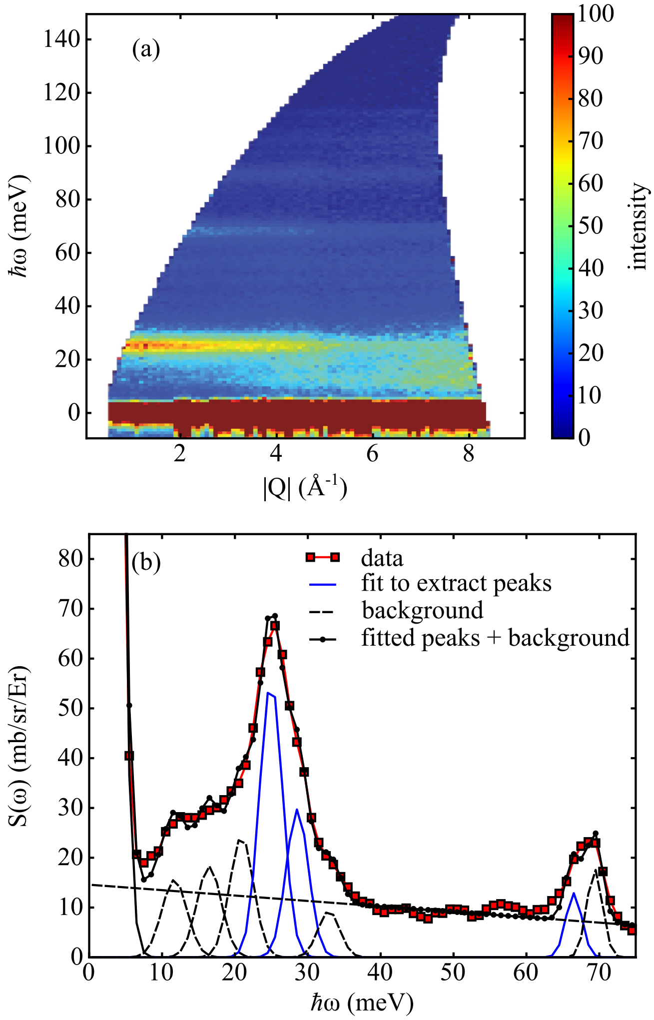

FIG. 4. High-energy neutron spectroscopy of pg-YbGO single-ion effects. Data are from SEQUOIA with $E_\mathrm{i} = 160\,\mathrm{meV}$ and $T = 5\,\mathrm{K}$. The isobar intensity values are in units of mb/sr/meV/Er.

with momentum as per the dipole approximation of the Yb^{3+} magnetic form factor [28]. The spectra were fit with a linear background plus a series of resolution limited Gaussians for both nonmagnetic and magnetic transitions. This fit of the $E_\mathrm{i} = 160\,\mathrm{meV}$, $T = 5\,\mathrm{K}$ intensities is shown in Fig. 4(b) with the extracted intensities reported in Table IV. Then, starting with the scaled parameters, a minimization of model residuals as described in Appendix A gave the calculated values in Table IV, with crystal field parameters reported in Table X of Appendix C. Unlike the pg-ErGO solution, the pg-YbGO optimization problem as posed has no quantification of uniqueness other than the agreement of the model with the available observables, and therefore no parameter uncertainties are reported.

The ground-state pg-YbGO wave function associated with the best fit, using the maximum anisotropy axis as the quantization axis, is a Kramer's doublet dominated by $m_\mathrm{J} = \pm 7/2$ with nonzero contributions of all other m_j values, as reported in Table XI of Appendix C. This solution yields a ground-state moment of 2.3 μ_B, which is larger than the 1.21 μ_B moment refined from the magnetic diffraction data at $T = 0.1\,\mathrm{K}$ reported in Table II and the discrepancy may be due diffraction data not being in the fully ordered state. These ground-state magnetic moments may be considered as local Ising from an energy scale consideration, as the first excited state is 283 K above the ground state with $T_\mathrm{N} < 1\,\mathrm{K}$.

TABLE IV. Crystal field levels in pg-YbGO at $T = 5\,\mathrm{K}$, $E_\mathrm{i} = 160\,\mathrm{meV}$. Data are averaged over $Q = [2, 4]\,\mathrm{Å}^{-1}$. Measured and calculated $S_\mathrm{CF}(\omega)$ have the momentum-dependent magnetic form factor contribution divided out. The uncertainties on measured quantities are one standard deviation confidence intervals from profiling the data in Fig. 4.

transition	measured $\hbar\omega$ (meV)	calculated $\hbar\omega$ (meV)	measured $S_\mathrm{CF}(\omega)$ (mb/sr/Yb)	calculated $S_\mathrm{CF}(\omega)$ (mb/sr/Yb)
$0 \rightarrow 1$	24.40 ± 0.04	24.6	315 ± 4	314.7
$0 \rightarrow 2$	27.86 ± 0.05	28.5	211 ± 3	224.9
$0 \rightarrow 3$	66.50 ± 0.05	66.5	52 ± 1	52.4

So, for both pg-ErGO and pg-YbGO, the pyrogermanate local environment stabilizes a large contribution of the maximal angular momentum state, but with finite mixing of other angular momentum states. Both compounds have large separations of the first excited state from the ground state, in comparison to the magnetic ordering energy scales, $E_{0\rightarrow1}/\mathrm{k_B T_N} = 99$ for pg-ErGO and $E_{0\rightarrow1}/\mathrm{k_B T_N} > 283$ for pg-YbGO. And so, the first condition of Ising behavior is well met for both compounds.

C. Ising spin-flip energy

Building upon the single-ion behavior, the energetics of the interacting ions of pg-ErGO and pg-YbGO in the magnetically ordered states can be probed with high-resolution neutron spectroscopy. In the magnetically ordered state, there will be additional transitions associated with flipping the putative local-Ising spins and potentially collective excitations. The incident neutrons may have either spin-flip ($\Delta S = \pm 1$) or non-spin-flip scattering processes ($\Delta S = 0$), so for a pure $m_\mathrm{J} = \pm J$ ground state there are no matrix elements connected by neutron scattering, but for the mixed wave functions produced by the low rare-earth site symmetry such neutron-induced transitions are nonzero.

The low-energy neutron spectra of pg-ErGO have features consistent with local-(quasi-)Ising magnetism, as seen in the temperature dependence (15 K, 1.5 K, 0.1 K) of $E_\mathrm{i} = 1.55\,\mathrm{meV}$ data in Fig. 5. Three features are observed in the energy spectrum: an elastic peak, a quasielastic response, and a dispersionless inelastic peak associated with spin flipping.

A quantitative visualization is possible by averaging over momentum transfer, as shown in Fig. 6. The spin-flipping (SF) mode is fit to a Gaussian and the quasielastic (QE) intensity is fit using a function corresponding to exponential decay of correlations in time [31] such that

$$S_\mathrm{QE}(\omega) = \frac{\chi'}{\pi}\frac{\omega\Gamma}{\omega^2 + \Gamma^2}\frac{1}{1 - e^{-\frac{\hbar\omega}{k_B T}}}\,, \tag{2}$$

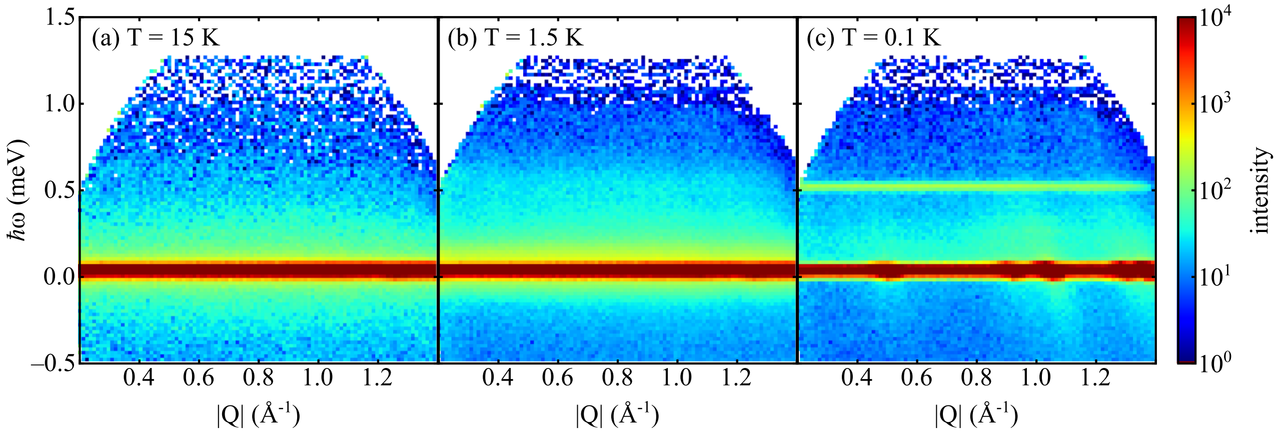

FIG. 5. Low-energy neutron spectroscopy of pg-ErGO in the ordered state. Data are from CNCS with $E_\mathrm{i} = 1.55\,\mathrm{meV}$. The isobar intensity values are in units of mb/sr/meV/Er. The data are shown on a logarithmic intensity scale.

where χ' is the susceptibility and $\hbar/\Gamma$ is a correlation time. At $T = 15\,\mathrm{K}$, which is well above T_N, QE excitations are present but no SF mode is observed. Cooling to $T = 1.5\,\mathrm{K}$, which is still above T_N, shows a broad SF peak and a reduction in the QE scattering. At $T = 0.1\,\mathrm{K}$ the SF peak is stronger and resolution limited, and the QE scattering is significantly decreased. These fitting results are reported in Table V. The observation of only one SF peak is due to only one symmetrically distinct Er^{3+} site in pg-ErGO. The persistence of QE scattering deep in the ordered state may be associated with some non-Ising character in pg-ErGO due to nonzero $\Delta S = \pm 1$ matrix elements from interactions between erbium ions or domain wall motion.

A similar analysis is possible for the magnetic excitations in the ordered state of pg-YbGO. The temperature dependence of the low-energy neutron spectra shows quasielastic intensity above and below the magnetic ordering temperature ($T < 1\,\mathrm{K}$), Fig. 7, with a much lower-energy spin-flip mode at approximately 0.07 meV. Averaging over momentum transfer shows the different aspects of the scattering more clearly, Fig. 8. These pg-YbGO data could not be fit using exponentially damped time correlations, as in Eq. (1). This Lorentzian fitting failure is due to the long tails in energy of a Lorentzian function that are not present in the data, as can be seen in Fig. 8 where the scattered intensity is negligible by ≈0.3 meV.

TABLE V. Low-energy excitations in pg-ErGO for $E_\mathrm{i} = 1.55\,\mathrm{meV}$. The quasielastic mode parameters are as in Eq. (2). The spin-flip mode parameters correspond to a Gaussian centered at E_SF, having a full-width-half-maximum of $\mathrm{FHWM}_\mathrm{SF}$, and integrating scattering function intensity of S_SF. Momentum dependence is averaged in the range from 0.2–0.8 $\mathrm{Å}^{-1}$.

T (K)	χ' (mb/sr/Er)	Γ (meV)	E_SF (meV)	$\mathrm{FHWM}_\mathrm{SF}$ (meV)	$S_\mathrm{SF}(\omega)$ (mb/sr/Er)
15	48.7	0.109			
1.5	291.9	0.109	0.477	0.202	1.3
0.1	245.5	0.109	0.477	0.026	6.8

Instead, a better fit was found to Gaussian time correlations:

$$S_\mathrm{QEG}(\omega) = \frac{\chi'\hbar\omega}{\sigma\sqrt{2\pi}} e^{-\frac{1}{2}(\hbar\omega/\sigma)^2} \frac{1}{1 - e^{-\frac{\hbar\omega}{k_B T}}}\,, \tag{3}$$

where χ' again plays the role of a susceptibility, but the frequency space and time space are modeled by Gaussian functions. Parameters from fits are reported in Table VI. There is a subtle inflection at $\hbar\omega = 0.17\,\mathrm{meV}$ that is not captured by a single Gaussian, most obvious in the 15 K data. This uncaptured inflection suggests that the interpretation as Gaussian time correlations may not be as simple as a zero-energy mode, but rather some highly damped finite energy mode(s). Such a model is not reported because a mode with an energy offset converged to zero energy offset during model optimization. The decrease in full-width-half-maximum of the quasielastic component at 1.5 K may be due to finite spin-flip intensity above the magnetic ordering temperature, as in

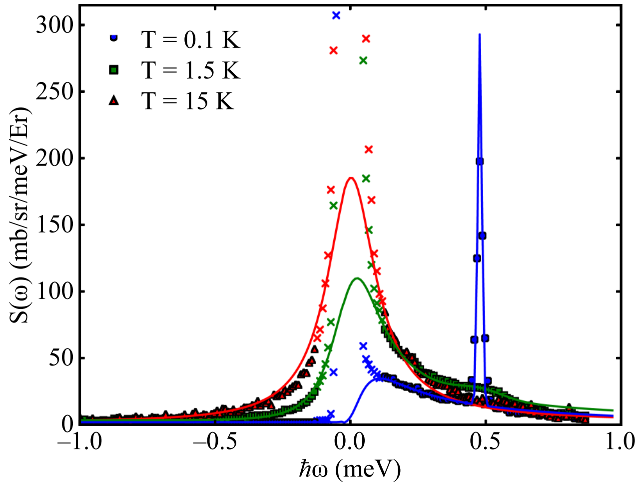

FIG. 6. Low-energy neutron spectroscopy of magnetic ordering effects in pg-ErGO. Data are from CNCS with $E_\mathrm{i} = 1.55\,\mathrm{meV}$. Momentum dependence is averaged in the range from 0.2–0.8 $\mathrm{Å}^{-1}$. The data displayed as x symbols were not included in the fitting of inelastic scattering. Lines are fits to Eq. (1).

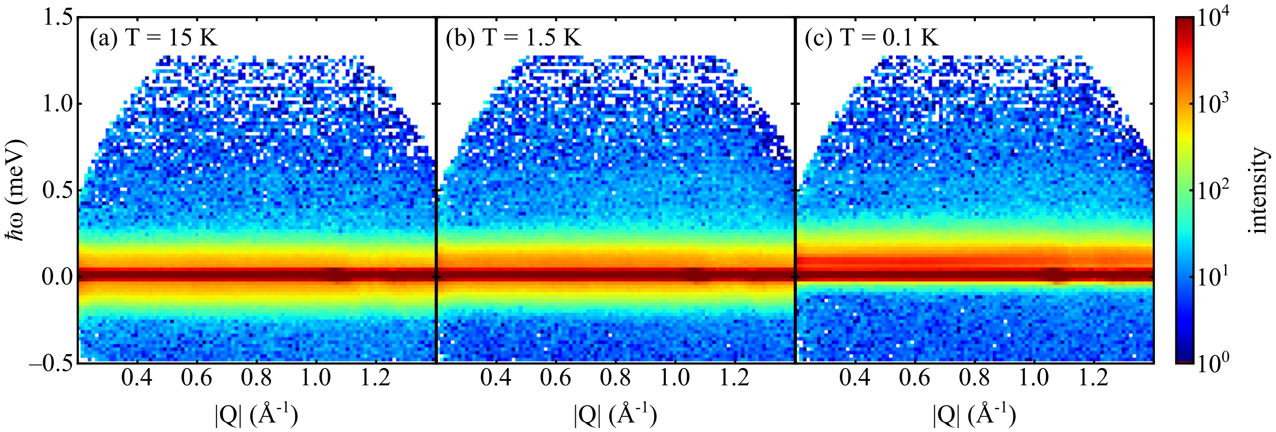

FIG. 7. Low-energy neutron spectroscopy of pg-ErGO in the ordered state. Data are from CNCS with $E_\mathrm{i} = 1.55\,\mathrm{meV}$. The isobar intensity values are in units of mb/sr/meV/Yb. The data are shown on a logarithmic intensity scale.

pg-ErGO. The spin-flip excitation in pg-YbGO is resolution limited in energy. The resolution function was not explicitly included in the quasielastic fit, but the resolution is highly linear over the region from –0.2 meV to 0.2 meV, varying from 0.044–0.033 meV, such that the FWHM$_\mathrm{QEG}$ values in Table VI may be adjusted for experimental effects by subtracting 0.038 meV.

It is striking that both pg-ErGO and pg-YbGO show dispersionless, resolution limited peaks associated with spin-flip transitions when cooled below their magnetic ordering temperatures. For both compounds, there is quasielastic scattering both above and below the magnetic ordering temperature. It is not clear if there is a fundamental reason why the pg-YbGO compound could not be fit well with exponential time correlations. Notably, pg-ErGO is entirely antiferromagnetic while pg-YbGO has a large ferromagnetic component and any spin diffusion is then expected to be different. Also, it may be that the inability to fit pg-YbGO quasielastic intensity with a single Lorentzian is due to an additional damping term.

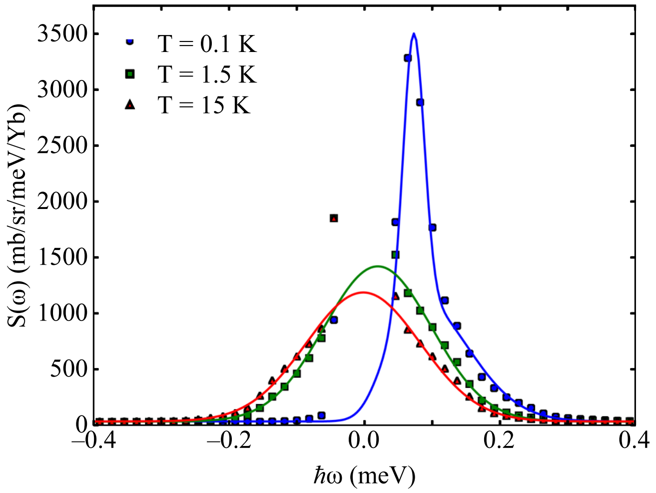

FIG. 8. Low-energy neutron spectroscopy of magnetic ordering effects in pg-YbGO. Data are from CNCS with $E_\mathrm{i} = 1.55\,\mathrm{meV}$. Momentum dependence is averaged in the range from 0.2–0.8 Å^{-1}. Lines are fits to Eq. (2).

D. Dipolar fields

For rare-earth-based magnets, the dipolar interactions are often dominant, although superexchange may be present [5]. For the pyrogermanates, a superexchange component is expected as the rare-earth polyhedral are edge sharing. Nevertheless, the magnetostatic contribution to magnetic interactions may be calculated from the reported magnetic crystal structure of pg-ErGO [19] and the pg-YbGO structure presented in Sec. II A. A semiclassical model that decorates the crystallographic lattice with magnetic moments of the experimentally determined magnitude gives rise to local magnetic fields of a magnitude $h_{\mathrm{dip,Er}} = 0.47\,\mathrm{T}$, and $h_{\mathrm{dip,Yb}} = 0.07\,\mathrm{T}$ for $m_{\mathrm{Yb}} = 1.21\,\mu_\mathrm{B}$ or $h_{\mathrm{dip,Yb}} = 0.14\,\mathrm{T}$ for $m_{\mathrm{yb}} = 2.3\,\mu_\mathrm{B}$. For pg-ErGO the erbium site with magnetic moment projections along the crystallographic axis $[a,b,c]$ of $\mathbf{m_{Er}} = [3.03\,\mu_\mathrm{B},\ 2.66\,\mu_\mathrm{B},\ –6.98\,\mu_\mathrm{B}]$, the dipolar magnetic field from the ordered lattice is $\mathbf{H_{dip,Er}} = [0.247\,\mathrm{T},\ 0.387\,\mathrm{T},\ –0.118\,\mathrm{T}]$, such that the angle between $\mathbf{m_{Er}}$ and $\mathbf{H_{dip,Er}}$ is 47.1°. Using these values, the semiclassical moment-flip energy of pg-ErGO is then calculated to be 0.30 meV. Using the wave functions for pg-ErGO from

TABLE VI. Low-energy excitations in pg-YbGO for $E_\mathrm{i} = 1.55\,\mathrm{meV}$. The quasielastic mode parameters are as in Eq. (3). The spin-flip mode parameters correspond to a Gaussian centered at E_{SF}, having a full-width-half-maximum of FHWM$_{\mathrm{SF}}$, and integrating scattering function intensity of S_{SF}. Momentum dependence is averaged in the range from 0.2–0.8 Å^{-1}.

T (K)	χ' (mb/sr/Yb)	FWHM$_{\mathrm{QEG}}$ (meV)	E_{SF} (meV)	FHWM$_{\mathrm{SF}}$ (meV)	$S_{\mathrm{SF}}(\omega)$ (mb/sr/Yb)
15	892.3	0.198			
1.5	10441.4	0.190			
0.1	19947.6	0.205	0.072	0.036	2442.9

the crystal field analysis and degenerate perturbation theory for the Hamiltonian associated with the local magnetic field, the off-diagonal elements have a small contribution and the energy splitting of the ground state is 0.32 meV (measured ground state splitting is 0.477 meV). The matrix elements of the local dipolar field are $\langle \mathrm{A}|\mathbf{m}_{\mathbf{Er}}\mathbf{H}_{\mathbf{dip},\mathbf{Er}}|\mathrm{A}\rangle = –0.16\,\mathrm{meV}$, $\langle \mathrm{B}|\mathbf{m}_{\mathbf{Er}}\mathbf{H}_{\mathbf{dip},\mathbf{Er}}\mathbf{J}|\mathrm{B}\rangle = 0.16\,\mathrm{meV}$, and $\langle \mathrm{A}|\mathbf{m}_{\mathbf{Er}}\mathbf{H}_{\mathbf{dip},\mathbf{Er}}\mathbf{J}|\mathrm{B}\rangle = \langle \mathrm{B}|\mathbf{m}_{\mathbf{Er}}\mathbf{H}_{\mathbf{dip},\mathbf{Er}}\mathbf{J}|\mathrm{A}\rangle = 0.03\,\mathrm{meV}$. For pure Ising interactions, the off-diagonal matrix elements would be zero, and for a pure Ising dipolar magnet the local dipolar fields would be parallel to the local quantization axes. For pg-YbGO, the dipolar magnetic field from the ordered lattice of $\mathbf{m}_{\mathbf{Yb}} = [0.31\,\mu_\mathrm{B},\ 0.09\,\mu_\mathrm{B},\ –1.17\,\mu_\mathrm{B}]$ is $\mathbf{H}_{\mathbf{dip},\mathbf{Yb}} = [–0.028\,\mathrm{T},\ 0.003\,\mathrm{T},\ –0.068\,\mathrm{T}]$, such that the angle between $\mathbf{m}_{\mathbf{Yb}}$ and $\mathbf{H}_{\mathbf{dip},\mathbf{Yb}}$ is 24.6°. The semiclassical moment-flip energy of pg-YbGO is then calculated to be 0.009 meV for $\mathrm{m}_{\mathrm{Yb}} = 1.21\,\mu_\mathrm{B}$ or 0.034 meV for $\mathrm{m}_{\mathrm{Yb}} = 2.3\,\mu_\mathrm{B}$ (measured ground-state splitting is 0.072 meV). Similarly to pg-ErGO, the degenerate perturbation theory calculation of the ground-state splitting due to a dipolar field in pg-YbGO modifies the semiclassical result by less than 10%. This underestimation in the magnetostatic model for both compounds implies that there is a molecular field due to superexchange that is of the same order of magnitude as the internal magnetic dipolar field.

Within the dipolar field model, there are a number of quantum phase transitions with applied magnetic field. There is a generic nature to such rich phase diagrams as in some other metamagnets [32], although the details are unique to pg-ErGO and pg-YbGO. For pg-ErGO, applying the magnetic field along a specific anisotropy axis will cause the local dimer to flip at an applied field of $h_{\mathrm{axis,dip}} = 0.47\,\mathrm{T}$ and give rise to net moments along all three crystallographic axes in four unique ways as there are four distinct local anisotropy axes. Applying a field along a given crystallographic axis will yield a net moment only along the applied field direction. A field that is geometrically between two local dimer axes will cause two dimers to go critical simultaneously in this model. All of these fields are anticipated to be less than 10 T (often $\sim$1 T) and therefore easily accessible with superconducting magnets, and some with permanent magnets. And so, the metamagnetic transition experimentally reported along the a axis at $\sim$0.35 T in pg-ErGO [19] is slightly larger than in the magnetostatic model but the overall picture is well captured. Similar considerations apply to pg-YbGO, with the modification that the ordered magnetic structure of pg-YbGO is ferromagnetic along the c axis. The multicritical points present in the pyrogermanates are a result of their complicated magnetic structures.

E. Non-Ising interaction terms

In regard to the second condition for Ising behavior, first consider the isotropic Heisenberg Hamiltonian where the spin-spin interaction that connects neighboring sites may be parameterized with

$$H_{\mathrm{Heisenberg}} = -J\sum_i\sum_\delta \left(S_i^x S_{i+\delta}^x + S_i^y S_{i+\delta}^y + S_i^z S_{i+\delta}^z\right) \tag{4}$$

or equivalently

$$H_{\mathrm{Heisenberg}} = -J\sum_i\sum_\delta \left(S_i^z S_{i+\delta}^z + \frac{1}{2}\left(S_i^+ S_{i+\delta}^- + S_i^- S_{i+\delta}^+\right)\right), \tag{5}$$

where the S operators now explicitly refer to spins and summations are as described in Eq. (1). For a paraxial system that satisfies the first Ising condition that the first excited Kramers doublet is well separated in energy from the ground state, the raising and lowering operators result in vacuum states and Eq. (5) formally reduces to the Ising model of Eq. (1). However, the details of the ground-state wave functions may cause non-Ising behavior even if the ground states are well separated from the first excited states. Moreover, dipolar interactions are long-range and may introduce interactions not even present in Eqs. (4) and (5), such as next-nearest-neighbor operators.

For the single-ion physics, it is useful to consider a local coordinate system where the J^z operators are diagonal. The Tables IX and X are for this local coordinate system of pg-ErGO, for which $\mathbf{m}_{\mathbf{Er},\mathbf{local}} = [0,\ 0,\ 8.5\,\mu_\mathrm{B}]$, and analogously the Tables XI and XII are for the different local coordinate system of pg-YbGO for which $\mathbf{m}_{\mathbf{Yb},\mathbf{local}} = [0,\ 0,\ 2.3\,\mu_\mathrm{B}]$. In these local coordinate systems, the J^y and J^x operators acting on the paramagnetic moments are zero for the ground-state doublets by design. For considering interactions between magnetic ions, a coordinate system common to all ions must be defined. For these pyrogermanates there is no coordinate system for which a J^z operator is diagonal for all ions in the unit cell, which is trivially deducible from the existence of local magnetization components having antiferromagnetic alignments without applied magnetic field. While a higher symmetry could exist where the interaction operators are still diagonal and Ising behavior is preserved, the finite angle between the local dipolar fields and local ordered moments means that this possible higher symmetry is not present for pg-ErGO and pg-YbGO.

This exercise of coordinate system rotation is shown representatively for the pg-ErGO parameters but is similarly calculable for pg-YbGO parameters. Taking the crystallographic coordinate system and the quantization axis of the local moments from the diffraction data, the resulting wave functions and crystal field operators are listed in Tables XII and XIII. The expectation values of the magnetic moments in the crystallographic system for the noninteracting single-ion wave functions are then $\mathbf{m}_{\mathbf{Er}} = [2.87\,\mu_\mathrm{B},\ 3.24\,\mu_\mathrm{B},\ –7.20\,\mu_\mathrm{B}]$ for one site, whereas the experimentally measured values via diffraction for that crystallographic site are $\mathbf{m}_{\mathbf{Er}} = [2.66\,\mu_\mathrm{B},\ 3.03\,\mu_\mathrm{B},\ –6.98\,\mu_\mathrm{B}]$ (from Table II) and the net dipolar field of the measured moments on that site is $\mathbf{H}_{\mathbf{dip},\mathbf{Er}} = [0.387\,\mathrm{T},\ 0.247\,\mathrm{T},\ –0.118\,\mathrm{T}]$. The other Er^{3+} sites are related by the symmetry operators of the magnetic structure. In general, the dipolar interaction has even more non-zero terms than the isotropic Heisenberg Hamiltonian, with nine different combinations of J^-, J^+, and J^z and six independent prefactors, although only Heisenberg XXZ-like terms survive for collinear moments [33]. A nearest-neighbor dipolar interaction Hamiltonian written in terms of the crystal coordinated system can be calculated corresponding to the three unique red, green, and blue distances in Fig. 1 by using the experimentally determined magnetic structures. Then, even considering only magnetostatic interactions, there will exist non-Ising dispersive modes due to nonzero raising and lowering operator expectation values of the ground-state doublet. Again, this violation of strict Ising behavior is experimentally confirmed by the nonzero transition in the ordered state induced by the neutron radiation that is a rank-1 tensor in angular momentum.

This line of thinking then concludes that to mitigate non-Ising contributions to the Hamiltonian of a so-called effective $J = 1/2$ material, the crystal system should have parallel quantization axes for the magnetic moments in question. As the angle between the dipolar magnetic field and the orientation of the ordered moment is more parallel in the pg-YbGO system, at least those magnetostatic interactions are more diagonal for the pg-YbGO than the pg-ErGO and better satisfying the second condition of Ising behavior.

III. CONCLUSIONS AND OPEN QUESTIONS

These results show that pyrogermanates have an Ising character, but additional non-Ising terms arise from the interactions between magnetic moments. The first criterion of the Ising model is well met by pg-ErGO and pg-YbGO, whereby there is a ground-state doublet well separated from the first excited state doublet with the ordering temperature setting the relevant energy scale. The large values of $E_{0\rightarrow1}/\mathrm{k_B T_N} = 99$ for pg-ErGO and $E_{0\rightarrow1}/\mathrm{k_B T_N} > 283$ for pg-YbGO put them in an elite class of materials measured by that metric. The second criterion of the Ising model requires a vanishing of off-diagonal matrix elements between neighboring sites, e.g., $\langle \mathrm{A}|h_{\mathrm{interaction}}|\mathrm{B}\rangle/\langle \mathrm{A}|h_{\mathrm{interaction}}|\mathrm{A}\rangle \rightarrow 0$ where $|\mathrm{A}\rangle$ and $|\mathrm{B}\rangle$ are the lowest-energy Kramers doublet wave functions. While quantitative details of the spin-spin interactions are not completely known, the nonvanishing off-diagonal matrix elements of the magnetostatic interaction suggests the potential for non-Ising behavior from this second criterion. The inelastic neutron scattering of the ordered state are dominated by a resolution-limited flat mode in energy, which is the fundamental excitation of a dispersionless Ising system, and coexisting with this Ising mode there is additional quasielastic scattering in the ordered state. We have quantified the quasielastic intensity, and while a microscopic model for these correlations is not completely determined there are now many observables to test such a model. For both Ising conditions, the pg-YbGO compound is more ideal, although the second condition was quantified with dipolar interactions and not superexchange. The magnetic structure of pg-YbGO was modeled and found to have a net ferromagnetic component, which is unique within the reported pyrogermanates.

Looking forward, rare-earth pyrogermanates may be a useful model system for testing the theory of magnetism and phase transitions. Single-crystal neutron scattering measurements in the ordered state may reveal dispersive modes and anisotropies hidden by powder averaging. Quantum multicritical points are anticipated with applied magnetic field, making these systems appropriate for studying universal behavior near multicritical points. Another interesting check will be to apply a magnetic field perpendicular to one of the local anisotropy axes to see if the ordered moment can be made to decrease at high fields. A doping series, such as $\mathrm{Er}_{2x}\mathrm{Y}_{2-2x}\mathrm{Ge}_2\mathrm{O}_7$ or $\mathrm{Yb}_{2x}\mathrm{Y}_{2-2x}\mathrm{Ge}_2\mathrm{O}_7$ may also be of interest where the effect of random fields on the magnetic state may be tested.

The Department of Energy will provide public access to these results of federally sponsored research in accordance with the DOE Public Access Plan [34].

ACKNOWLEDGMENTS

D.M.P., K.M.T., A.T.S., and M.B.S. are supported through the Scientific User Facilities Division of the Department of Energy (DOE) Office of Science, sponsored by the Basic Energy Science (BES) Program, DOE Office of Science. L.D.S. is supported by the U.S. Department of Energy (DOE), Office of Science, Basic Energy Sciences (BES), Materials Science and Engineering Division. This research used resources at the High Flux Isotope Reactor and Spallation Neutron Source, a DOE Office of Science User Facility operated by the Oak Ridge National Laboratory. The material synthesis and crystal growth at Clemson was supported by DOE BES award DE-SC0020071. Andrey Podlesnyak, Steve Nagler, Garrett Granroth, and Mark Lumsden helped to discuss these data. Doug Armitage assisted in design of the sample holder for the CNCS experiment. Todd Sherline operated the refrigerator for the CNCS experiment. This manuscript has been authored by UT-Battelle, LLC under Contract No. DE-AC05-00OR22725 with the U.S. Department of Energy. The United States Government retains and the publisher, by accepting the article for publication, acknowledges that the United States Government retains a nonexclusive, paid-up, irrevocable, worldwide license to publish or reproduce the published form of this manuscript, or allow others to do so, for United States Government purposes.

APPENDIX A: TECHNICAL DETAILS

These powder samples were synthesized from the solid state using total mass 5 g, 2:1 stoichiometric ratio mixtures of GeO_2 and $\mathrm{Er}_2\mathrm{O}_3$ or $\mathrm{Yb}_2\mathrm{O}_3$ for pg-ErGO or pg-YbGO, respectively. The reactants were mixed, ground, and heated to 1000 °C for 12 h. The powder products were pressed into pellets and calcined at 1250 °C for 24 h. Heating and regrinding was iterated until no impurities were observed with diffraction. The pg-ErGO samples examined here are from the same batch as the powder diffraction study [19]. For the SEQUOIA experiments, samples were mounted in cylindrical aluminum cans of 1 cm diameter, sealed with indium in a helium atmosphere. Cooling was achieved with the SEQUOIA top-loading CCR. Chopper settings for the $E_\mathrm{i} = 160\,\mathrm{meV}$ data used the high-resolution Fermi chopper, with $\mathrm{T0} = 120\,\mathrm{Hz}$, $\mathrm{F1} = 120\,\mathrm{Hz}$, and $\mathrm{F2} = 600\,\mathrm{Hz}$. For the CNCS experiments, samples were mounted in flat plates of 0.5 mm thick having copper bodies and 0.635 mm thick aluminum windows. Flat plate surface normals were 45° with respect to the incident beam, e.g., $2\theta = 90^\circ$. Flat plate absorption corrections were calculated and applied to the CNCS diffraction data. The

Triton-NANO dilution refrigerator was used for cooling the sample. Chopper settings for the $E_\mathrm{i} = 1.55$ meV data used the high-flux double-disk opening, with a Fermi chopper frequency of 60 Hz, and a double-disk frequency of 300 Hz. Normalization of data between the CNCS and the SEQUOIA spectrometers was done by using the incoherent integrated intensity averaged from $Q = 0.2$ Å^{-1} to $Q = 0.8$ Å^{-1}. For pg-YbGO powder diffraction with HB2a at the High Flux Isotope Reactor, samples were mounted in copper cans and cooled in a dilution refrigerator. Experimental energy resolutions and crystal field calculations are from MANTID [35]. Dipolar field calculations were performed by taking a site at the center of a 10 × 10 × 10 supercell. Magnetic diffraction was modeled following the methodology and notations used in reference [19], utilizing the programs FULLPROF [36] and SARAh [37]. For fitting the CNCS data, a downhill simplex algorithm was used. For crystal field fitting, a downhill simplex algorithm was initially used. The best-fit solution was then subjected to basin-hopping, differential evolution, and simulated annealing algorithms in an attempt to find a more global solution but ultimately without any decrease in χ^2. These solutions were then subjected to Levenberg-Marquardt minimization to extract [38] confidence intervals. For derived parameters, such as the wave-function coefficients, parameter populations were created with normal distributions defined by the mean and standard deviations of the fits. These parameter populations were then sampled and statistical analysis was then performed on the resulting data.

APPENDIX B: pg-YbGO STRUCTURAL REFINEMENT

Powder diffraction of pg-YbGO was measured on the Hb-2A diffractometer of the High Flux Isotope Reactor using an incident wavelength of 2.41 Å, Fig. 9. While the thermometer on the mixing chamber of the dilution refrigerator for the $T < 1$ K data was 50 mK, subsequent diagnostics of the mounting geometry showed the sample temperature to be unquantifiably between 50 mK and 1 K.

TABLE VII. Crystallographic parameters of pg-YbGO at 10 K and <1 K.

Temperature (K) Space group	10 $P4_12_12$	<1 $P4_12_12$
R_{wp}		
a (Å)	6.7402(1)	6.7402(1)
c (Å)	12.2613(1)	12.2611(1)
c/a	1.8193(1)	1.8191(1)
V (Å)	557.03(1)	557.03(1)
Yb (8b)		
x	0.874(1)	0.875(1)
y	0.355(1)	0.356(1)
z	0.136(1)	0.136(1)
U	0.001(1)	0.0001(1)
Ge (8b)		
x	0.899(1)	0.899(1)
y	0.153(1)	0.153(1)
z	0.618(1)	0.618(1)
U	0.0001	0.0001(1)
O1 (4a)		
x	0.804(1)	0.805(1)
y	0.196(1)	0.195(1)
z	0.750	0.750
U	0.004(1)	0.003(1)
O2 (8b)		
x	0.077(1)	0.077(1)
y	−0.035(1)	−0.035(1)
z	0.622(1)	0.622(1)
U	0.004(1)	0.003(1)
O3 (8b)		
x	0.064(1)	0.064(1)
y	0.335(1)	0.335(1)
z	0.572(1)	0.572(1)
U	0.004(1)	0.003(1)
O4 (8b)		
x	0.680(1)	0.680(1)
y	0.142(1)	0.143(1)
z	0.542(1)	0.543(1)
U	0.004(1)	0.003(1)

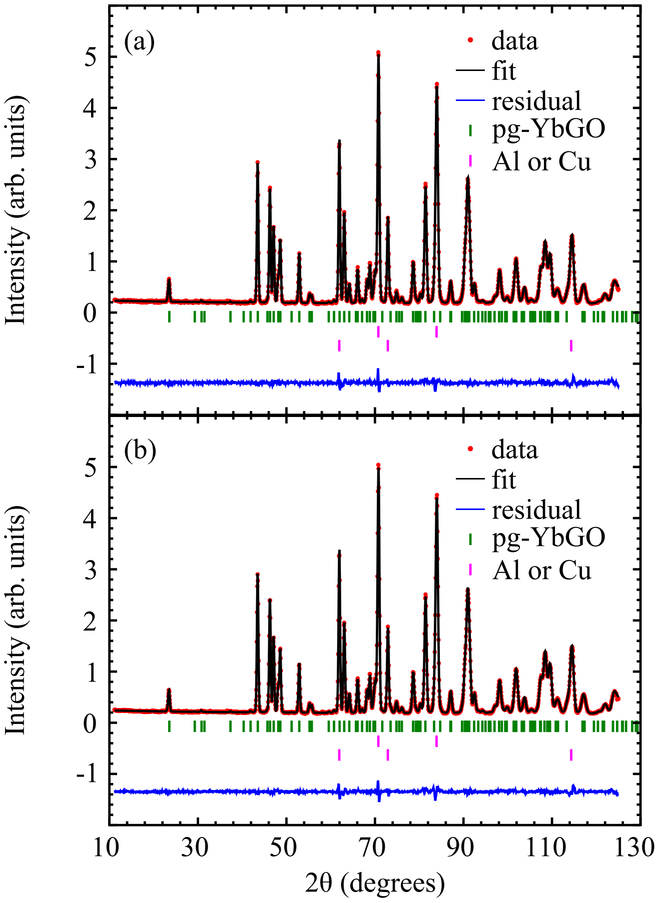

FIG. 9. Neutron powder diffraction of pg-YbGO. Temperatures of (a) 10 K and (b) <1 K are shown. The Al and Cu contributions are from the equipment holding the sample.

APPENDIX C: CRYSTAL FIELD PARAMETERS

The crystal field Hamiltonian $B_{\ell m}$ parameters are listed here along with the wave-function fractions. The notation Re and Im denote real and imaginary components. The ℓ and m are from spherical harmonics. The $|A\rangle$ and $|B\rangle$ are the two energetically degenerate members of the ground-state Kramer's doublet in the paramagnetic state.

TABLE VIII. Crystal field $B_{\ell m}$ parameters for pg-ErGO with the quantization axis defined locally to be maximal for the J^z operator for the ground state. The standard deviation confidence intervals are from model fitting.

	$\ell = 2$ (meV)	$\ell = 4$ (meV)	$\ell = 6$ (meV)
Im$\{m = 6\}$			$-2.24 \times 10^{-5} \pm 0.49 \times 10^{-5}$
Im$\{m = 5\}$			$-9.50 \times 10^{-5} \pm 1.37 \times 10^{-5}$
Im$\{m = 4\}$		$-5.41 \times 10^{-3} \pm 0.11 \times 10^{-3}$	$1.28 \times 10^{-5} \pm 0.33 \times 10^{-5}$
Im$\{m = 3\}$		$-5.73 \times 10^{-3} \pm 1.16 \times 10^{-3}$	$-4.35 \times 10^{-5} \pm 1.32 \times 10^{-5}$
Im$\{m = 2\}$	0.015 ± 0.009	$-1.66 \times 10^{-3} \pm 0.24 \times 10^{-3}$	$3.54 \times 10^{-5} \pm 0.55 \times 10^{-5}$
Im$\{m = 1\}$	0.068 ± 0.029	$-1.12 \times 10^{-3} \pm 0.39 \times 10^{-3}$	$1.30 \times 10^{-5} \pm 0.45 \times 10^{-5}$
$m = 0$	-0.201 ± 0.003	$-0.40 \times 10^{-3} \pm 0.01 \times 10^{-3}$	$0.07 \times 10^{-5} \pm 0.01 \times 10^{-5}$
Re$\{m = 1\}$	0.209 ± 0.028	$0.29 \times 10^{-3} \pm 0.22 \times 10^{-3}$	$-3.81 \times 10^{-5} \pm 0.37 \times 10^{-5}$
Re$\{m = 2\}$	-0.156 ± 0.016	$0.76 \times 10^{-3} \pm 0.05 \times 10^{-3}$	$-0.64 \times 10^{-5} \pm 0.33 \times 10^{-5}$
Re$\{m = 3\}$		$12.34 \times 10^{-3} \pm 1.54 \times 10^{-3}$	$0.20 \times 10^{-5} \pm 1.02 \times 10^{-5}$
Re$\{m = 4\}$		$-0.56 \times 10^{-3} \pm 0.78 \times 10^{-3}$	$1.37 \times 10^{-5} \pm 0.67 \times 10^{-5}$
Re$\{m = 5\}$			$-15.35 \times 10^{-5} \pm 3.32 \times 10^{-5}$
Re$\{m = 6\}$			$2.94 \times 10^{-5} \pm 0.74 \times 10^{-5}$

TABLE IX. Ground-state wave functions for pg-ErGO with the quantization axis defined locally to be maximal for the J^z operator for the ground state. The standard deviation confidence intervals are from model fitting.

	Re$\{\|A\rangle\}$	Im$\{\|A\rangle\}$	Re$\{\|B\rangle\}$	Im$\{\|B\rangle\}$
$m_j = -7.5$	0.9335 ± 0.0002	0.0 ± 0.0	0.0000 ± 0.0039	0.0 ± 0.0
$m_j = -6.5$	-0.0773 ± 0.0008	0.0717 ± 0.0007	0.0037 ± 0.0009	-0.0036 ± 0.0010
$m_j = -5.5$	0.0458 ± 0.0002	0.1725 ± 0.0003	0.0225 ± 0.0019	-0.0069 ± 0.0058
$m_j = -4.5$	0.1494 ± 0.0001	0.2123 ± 0.0001	-0.0133 ± 0.0008	-0.0014 ± 0.0033
$m_j = -3.5$	-0.0039 ± 0.0003	-0.0201 ± 0.0003	-0.0052 ± 0.0054	-0.0216 ± 0.0015
$m_j = -2.5$	-0.0174 ± 0.0002	0.0796 ± 0.0001	0.0067 ± 0.0024	0.0095 ± 0.0018
$m_j = -1.5$	0.0344 ± 0.0002	0.0107 ± 0.0002	-0.0453 ± 0.0068	-0.0263 ± 0.0114
$m_j = -0.5$	0.0328 ± 0.0001	-0.0563 ± 0.0002	-0.0280 ± 0.0045	0.0178 ± 0.0071
$m_j = +0.5$	-0.0289 ± 0.0003	-0.0184 ± 0.0002	-0.0316 ± 0.0138	-0.0548 ± 0.0081
$m_j = +1.5$	0.0469 ± 0.0001	-0.0270 ± 0.0002	0.0335 ± 0.0028	-0.0102 ± 0.0084
$m_j = +2.5$	0.0070 ± 0.0003	-0.0098 ± 0.0003	0.0165 ± 0.0194	0.0773 ± 0.0047
$m_j = +3.5$	0.0055 ± 0.0001	-0.0223 ± 0.0001	-0.0039 ± 0.0049	0.0195 ± 0.0012
$m_j = +4.5$	-0.0134 ± 0.0009	0.0016 ± 0.0009	-0.1457 ± 0.0517	0.2052 ± 0.0371
$m_j = +5.5$	-0.0234 ± 0.0007	-0.0073 ± 0.0006	0.0451 ± 0.0420	-0.1671 ± 0.0122
$m_j = +6.5$	0.0039 ± 0.0004	0.0037 ± 0.0004	0.0747 ± 0.0177	0.0698 ± 0.0189
$m_j = +7.5$	-0.0002 ± 0.0029	-0.0012 ± 0.0036	0.9050 ± 0.0250	0.0038 ± 0.2275

TABLE X. Crystal field $B_{\ell m}$ parameters for pg-YbGO with the quantization axis defined locally to be maximal for the J^z operator for the ground state.

	$\ell = 2$ (meV)	$\ell = 4$ (meV)	$\ell = 6$ (meV)
Im$\{m = 6\}$			-97.03×10^{-5}
Im$\{m = 5\}$			232.67×10^{-5}
Im$\{m = 4\}$		61.14×10^{-3}	-33.28×10^{-5}
Im$\{m = 3\}$		40.68×10^{-3}	160.77×10^{-5}
Im$\{m = 2\}$	-0.052	-27.90×10^{-3}	-15.8×10^{-5}
Im$\{m = 1\}$	0.204	38.61×10^{-3}	-9.46×10^{-5}
$m = 0$	-0.249	-19.15×10^{-3}	-13.17×10^{-5}
Re$\{m = 1\}$	0.837	167.58×10^{-3}	70.37×10^{-5}
Re$\{m = 2\}$	-0.098	16.22×10^{-3}	22.87×10^{-5}
Re$\{m = 3\}$		251.41×10^{-3}	-164.54×10^{-5}
Re$\{m = 4\}$		122.03×10^{-3}	109.03×10^{-5}
Re$\{m = 5\}$			529.82×10^{-5}
Re$\{m = 6\}$			261.87×10^{-5}

TABLE XI. Ground-state wave functions for pg-YbGO with the quantization axis defined locally to be maximal for the J^z operator for the ground state.

	$\mathrm{Re}\{\lvert A\rangle\}$	$\mathrm{Im}\{\lvert A\rangle\}$	$\mathrm{Re}\{\lvert B\rangle\}$	$\mathrm{Im}\{\lvert B\rangle\}$
$m_j = -3.5$	0.7697	0.0	−0.0067	0.0
$m_j = -2.5$	0.3174	−0.0523	−0.1156	0.0437
$m_j = -1.5$	−0.1938	−0.0232	0.0858	0.1289
$m_j = -0.5$	0.3476	−0.0246	−0.2621	−0.1910
$m_j = +0.5$	−0.3079	0.1018	−0.3235	−0.1295
$m_j = +1.5$	−0.1210	0.0966	−0.1916	−0.0371
$m_j = +2.5$	−0.0968	−0.0769	−0.2862	−0.1467
$m_j = +3.5$	0.0064	0.0020	0.7330	0.2350

TABLE XII. Crystal field $B_{\ell m}$ parameters for one Er^{3+} site in pg-ErGO with the quantization axis defined in the crystallographic coordinate system. These values parameterize an Er^{3+} site with magnetic moment expectation values of $m_{Er} = [\pm 2.87\,\mu_B,\ \pm 3.24\,\mu_B,\ \mp 7.20\,\mu_B]$.

	$\ell = 2$ (meV)	$\ell = 4$ (meV)	$\ell = 6$ (meV)
$\mathrm{Im}\{m = 6\}$			1.08×10^{-5}
$\mathrm{Im}\{m = 5\}$			2.77×10^{-5}
$\mathrm{Im}\{m = 4\}$		6.08×10^{-3}	-0.71×10^{-5}
$\mathrm{Im}\{m = 3\}$		-4.87×10^{-3}	7.18×10^{-5}
$\mathrm{Im}\{m = 2\}$	−0.167	-3.18×10^{-3}	3.19×10^{-5}
$\mathrm{Im}\{m = 1\}$	0.235	0.17×10^{-3}	1.51×10^{-5}
$m = 0$	−0.188	-0.13×10^{-3}	0.20×10^{-5}
$\mathrm{Re}\{m = 1\}$	0.189	0.67×10^{-3}	-4.56×10^{-5}
$\mathrm{Re}\{m = 2\}$	−0.034	0.69×10^{-3}	0.52×10^{-5}
$\mathrm{Re}\{m = 3\}$		5.54×10^{-3}	-1.69×10^{-5}
$\mathrm{Re}\{m = 4\}$		-1.42×10^{-3}	-0.85×10^{-5}
$\mathrm{Re}\{m = 5\}$			-10.19×10^{-5}
$\mathrm{Re}\{m = 6\}$			-2.63×10^{-5}

TABLE XIII. Ground-state wave functions for one Er^{3+} site in pg-ErGO with the quantization axis defined in the crystallographic coordinate system. These values parameterize an Er^{3+} site with magnetic moment expectation values of $m_{Er} = [\pm 2.87\,\mu_B,\ \pm 3.24\,\mu_B,\ \mp 7.20\,\mu_B]$.

	$\mathrm{Re}\{\lvert A\rangle\}$	$\mathrm{Im}\{\lvert A\rangle\}$	$\mathrm{Re}\{\lvert B\rangle\}$	$\mathrm{Im}\{\lvert B\rangle\}$
$m_j = -7.5$	0.5337	0.0	0.0333	0.0
$m_j = -6.5$	0.0035	−0.5728	0.0131	−0.0618
$m_j = -5.5$	−0.2242	−0.4053	0.0118	−0.0285
$m_j = -4.5$	−0.2780	−0.1516	−0.0494	−0.0071
$m_j = -3.5$	−0.1900	0.0689	−0.0026	−0.0176
$m_j = -2.5$	−0.0013	−0.0181	0.0180	0.0149
$m_j = -1.5$	0.0536	−0.0511	0.0274	0.0047
$m_j = -0.5$	0.0061	−0.0981	−0.0402	−0.0645
$m_j = +0.5$	−0.0196	−0.0734	0.0758	0.0626
$m_j = +1.5$	0.0153	−0.0232	−0.0740	0.0042
$m_j = +2.5$	−0.0014	0.0233	0.0123	0.0134
$m_j = +3.5$	0.0110	0.0140	0.1801	−0.0917
$m_j = +4.5$	0.0286	−0.0410	−0.0792	0.3067
$m_j = +5.5$	0.0286	0.0109	−0.1429	−0.4405
$m_j = +6.5$	−0.0541	−0.0326	0.4207	0.3887
$m_j = +7.5$	0.0228	−0.0243	−0.3645	0.3898

---

[1] S. G. Brush, Rev. Mod. Phys. **39**, 883 (1967).

[2] S. Lloyd, Science **273**, 1073 (1996).

[3] M. J. Jozef Strečka, Acta Phys. Slovaca **65**, 235 (2015).

[4] W. P. Wolf, Brazilian J. Phys. **30**, 794 (2000).

[5] R. L. Carlin, *Magnetochemistry* (Springer-Verlag, Berlin, 1986).

[6] J. A. A. Ketelaar, Physica **4**, 619 (1937).

[7] A. H. Cooke, D. T. Edmonds, C. B. P. Finn, and W. P. Wolf, Proc. R. Soc. London. Ser. A **306**, 335 (1968).

[8] P. G. Dawber, C. B. P. Finn, and H. Jamshidi, J. Phys. C Solid State Phys. **17**, 6735 (1984).

[9] E. Lagendijk, H. W. J. Blöte, and W. J. Huiskamp, Physica **61**, 220 (1972).

[10] B. C. Gerstein, C. J. Penney, and F. H. Spedding, J. Chem. Phys. **37**, 2610 (1962).

[11] J. Xu, M. R. Roser, and L. R. Corruccini, J. Low Temp. Phys. **78**, 13 (1990).

[12] A. H. Cooke, F. R. McKim, H. Meyer, and W. P. Wolf, Philos. Mag. **2**, 928 (1957).

[13] E. J. Graeber, G. H. Conrad, and S. F. Duliere, Acta Crystallogr. **21**, 1012 (1966).

[14] W. J. Huiskamp and E. Lagendijk, Physica **65**, 118 (1973).

[15] L. Couture and K. Rajnak, Chem. Phys. **85**, 315 (1984).

[16] J. S. Gardner, M. J. P. Gingras, and J. E. Greedan, Rev. Mod. Phys. **82**, 53 (2010).

[17] Y. I. Smolin, Sov. Phys. - Crystallogr. **15**, 36 (1970).

[18] B. M. Wanklyn, J. Mater. Sci. **8**, 649 (1973).

[19] K. M. Taddei, L. Sanjeewa, J. W. Kolis, A. S. Sefat, C. De La Cruz, and D. M. Pajerowski, Phys. Rev. Mater. **3**, 014405 (2019).

[20] M. Wardzyńska and B. M. Wanklyn, Phys. Status Solidi **40**, 663 (1977).

[21] R. J. Elliott, editor, *Magnetic Properties of Rare Earth Metals* (Plenum Press, London, 1972).

[22] M. Ghosh, S. Jana, D. Ghosh, and B. M. Wanklyn, Solid State Commun. **107**, 113 (1998).

[23] X. Ke, M. L. Dahlberg, E. Morosan, J. A. Fleitman, R. J. Cava, and P. Schiffer, Phys. Rev. B **78**, 104411 (2008).

[24] E. Morosan, J. A. Fleitman, Q. Huang, J. W. Lynn, Y. Chen, X. Ke, M. L. Dahlberg, P. Schiffer, C. R. Craley, and R. J. Cava, Phys. Rev. B **77**, 224423 (2008).

[25] K. Momma and F. Izumi, J. Appl. Crystallogr. **44**, 1272 (2011).

[26] See Supplemental Material at http://link.aps.org/supplemental/10.1103/PhysRevB.101.014420 for an mcif file containing the pg-YbGO magnetic structure.

[27] J. M. Cadogan, D. H. Ryan, G. A. Stewart, and R. Gagnon, J. Magn. Magn. Mater. **265**, 199 (2003).

[28] H. Börner, J. Brown, C. J. Carlile, R. Cubitt, R. Currat, A. J. Dianoux, B. Farago, A. W. Hewat, J. Kulda, E. Lelièvre-Berna, G. J. McIntyre, S. A. Mason, R. P. May, A. Oed, J. R. Stewart, F. Tasset, J. Tribolet, I. Anderson, and D. W. Dubbers, *Neutron Data Booklet* (Old City Publishing, Philadelphia, 2003).

[29] S. Edvardsson and M. Klintenberg, J. Alloys Compd. **275–277**, 230 (1998).

[30] Y. M. Jana, M. Ghosh, D. Ghosh, and B. M. Wanklyn, J. Magn. Magn. Mater. **210**, 93 (2000).

[31] G. Shirane, S. Shapiro, and J. Tranquada, *Neutron Scattering with a Triple-Axis Spectrometer* (Cambridge University Press, Cambridge, 2004).

[32] E. Stryjewski and N. Giordano, Adv. Phys. **26**, 487 (1977).

[33] B. Cowan, *Nuclear Magnetic Resonance and Relaxation* (Cambridge University Press, New York, 1997).

[34] http://energy.gov/downloads/doe-public-access-plan

[35] O. Arnold, J. C. Bilheux, J. M. Borreguero, A. Buts, S. I. Campbell, L. Chapon, M. Doucet, N. Draper, R. Ferraz Leal, M. A. Gigg, V. E. Lynch, A. Markvardsen, D. J. Mikkelson, R. L. Mikkelson, R. Miller, K. Palmen, P. Parker, G. Passos, T. G. Perring, P. F. Peterson, S. Ren, M. A. Reuter, A. T. Savici, J. W. Taylor, R. J. Taylor, R. Tolchenov, W. Zhou, and J. Zikovsky, Nucl. Instruments Methods Phys. Res. Sect. A: Accel. Spectrometers, Detect. Assoc. Equip. **764**, 156 (2014).

[36] J. Rodríguez-Carvajal, Phys. B: Condens. Matter **192**, 55 (1993).

[37] A. S. Wills, Phys. B: Condens. Matter **276–278**, 680 (2000).

[38] E. Jones, T. Oliphant, and P. Peterson, SciPy Open Source Sci. Tools Python, arXiv:1907.10121.